Atomistic Modeling of Crystal-to-Amorphous Transition and Associated Kinetics in the Ni−Nb System by Molecular Dynamics Simulations

X. D. Dai, J. H. Li, and B. X. Liu*

Advanced Materials Laboratory, Department of Materials Science and Engineering, Tsinghua University, Beijing 100084, China, and State Key Lab of Solid-State Microstructure, Nanjing University, Nanjing 200093, China

With the aid of ab initio calculations, an *n*-body potential of the Ni−Nb system is constructed under the Finnis−Sinclair formalism and the constructed potential is capable of not only reproducing some static physical properties but also revealing the atomistic mechanism of crystal-to-amorphous transition and associated kinetics. With application of the constructed potential, molecular dynamics simulations using the solid solution models reveal that the physical origin of crystal-to-amorphous transition is the crystalline lattice collapsing while the solute atoms are exceeding the critical solid solubilities, which are determined to be 19 atom % Ni and 13 atom % Nb for the Nb- and Ni-based solid solutions, respectively. It follows that an intrinsic glass-forming ability of the Ni−Nb system is within 19−87 atom % Ni, which matches well with that observed in ion beam mixing/solid-state reaction experiments. Simulations using the Nb/Ni/Nb (Ni/Nb/Ni) sandwich models indicate that the amorphous layer at the interfaces grows in a layer-by-layer mode and that, upon dissolving solute atoms, the Ni lattice approaches and exceeds its critical solid solubility faster than the Nb lattice, revealing an asymmetric behavior in growth kinetics. Moreover, an energy diagram is obtained by computing the energetic sequence of the $Ni_xNb_{100−x}$ alloy in fcc, bcc, and amorphous structures, respectively, over the entire composition range, and the diagram could serve as a guide for predicting the metastable alloy formation in the Ni−Nb system.

I. Introduction

The first amorphous alloy (or metallic glass) was obtained in 1959 by P. Duwez et al. using liquid melt quenching (LMQ) to freeze an Au−Si alloy in its liquid state from the melt,[1] which, from a nature science point of view, was the discovery of a new state of matter, that is, the amorphous solid,[2] while, from a materials science point of view, was the birth of a new field of metallic glasses.[3] In the early 1980s, a powerful method, that is, ion beam mixing (IBM) of multiple metal layers, was developed, and numerous amorphous alloys have since been produced in a great number of binary metal systems to date. Because of its high capability, IBM is even able to produce metallic glasses in some equilibrium immiscible systems, in which LMQ is not able to co-melt the two constituent metals to form any alloy,[4,5] yet has so far not succeeded in obtaining amorphous alloys in some other systems, for example, the Ni−Ru system, which has a peritectic phase diagram at equilibrium.[6] A very basic issue has hereby been raised, that is, in which system and at what composition(s) an amorphous alloy could be obtained. In other words, one of the fundamental issues in the field is to clarify the physical origin of the crystal-to-amorphous transition as well as to predict the glass-forming ability/range (GFA/GFR) of a binary metal system.[7−11]

In the past decades, several empirical criteria and models, mainly based on the physical−chemical properties of a system or the constituent metals, have been proposed. Among them, the most successful one is the structural difference rule, which was based on considering the crystalline structure, atomic size,

and electronegativity of the constituent metals, and its later extension by defining a single parameter, namely, the maximum possible amorphization range (MPAR) to predict the GFA/GFR of a system.[12−14] The physical meaning is that the MPAR corresponds to the total width of the two-phase region(s), in which amorphous alloy formation is favored, and accordingly, MPAR is equal to 100%, which represents the entire composition range, minus the two maximum terminal solid solubilities observed from the equilibrium phase diagram of the system. Although the prediction based on the empirical parameter MPAR has been quite successful, an obvious problem is that the maximum terminal solid solubilities are of equilibrium values, whereas the production of the amorphous alloys is certainly under a process of nonequilibrium or even far-from-equilibrium. Apparently, one should take into account the nonequilibrium solid solubilities to predict the GFA/GFR of a system. In fact, the present authors' group has recently revealed that the GFA/GFR of a system is indeed directly related to the two critical solid solubilities of the terminal supersaturated (i.e., nonequilibrium) solid solutions, which can directly be evaluated from a realistic interatomic potential of the system through molecular dynamics (MD) simulation.[15]

Also, in the early 1980s, another type of crystal-to-amorphous transition has been observed in the binary metal systems, that is, the first solid-state amorphization (SSA) taking place in the Au−La multilayered films reported by Schwarz and Johnson.[16] Since then, SSA has extensively been studied. For example, SSA has been observed not only in some systems having large negative heats of formation but also in some systems having small negative heats of formation, for example, in the Ni−Mo system or even in the equilibrium immiscible systems (e.g., the

* To whom correspondence should be addressed. E-mail: dmslbx@tsinghua.edu.cn.

Cu−Ta system with a positive heat of formation).[17−19] In experimental studies, an interesting phenomenon, that is, an asymmetric growth of the amorphous interlayer during SSA, has been observed in the Zr−Ni and Zr−Co bilayered films.[20,21] For example, in a cross-sectional Co−Zr bilayer sample, the amorphous interlayer grew by consuming Co and Zr at two different speeds with an estimated ratio of ∼2:1. In this respect, however, theoretical modeling concerning the detailed growth kinetics of SSA, especially at an atomic scale, needs much further investigation. In the present study, we dedicate ourselves to developing atomistic modeling for clarifying the underlying physics of crystal-to-amorphous transition and the associated asymmetric growth kinetics in a representative system, that is, the Ni−Nb system, by first deriving a realistic *n*-body Ni−Nb potential and then performing molecular dynamics (MD) simulation.

To our knowledge, there has been a published Ni−Nb potential based on the embedded-atom method (EAM),[22] which, however, was not able to reproduce the experimentally observed crystal-to-amorphous transition in the Ni−Nb multilayers.[23,24] Consequently, to develop atomistic modeling for the Ni−Nb system, we first reconstruct an *n*-body Ni−Nb potential based on the Finnis−Sinclair (FS) formalism[25] with the aid of ab initio calculations to acquire some physical properties for deriving the Ni−Nb cross-potential. Second, after proving the relevance of the derived Ni−Nb potential, MD simulations are performed using the solid solution models to reveal the physical mechanism of the crystal-to-amorphous transition as well as to determine the GFA/GFR of the Ni−Nb system. In performing the simulations, the main idea is to compare the relative stability of the solid solution versus its amorphous counterpart over the entire composition range, thus determining the two critical solid solubilities, at and beyond which the solid solutions become unstable and turn into the corresponding amorphous states. Third, MD simulations are also performed using the sandwich models to closely examine the interfacial reaction at the Ni/Nb interfaces for revealing the detailed kinetics of the resultant solid-state amorphization. Moreover, the correlation between the structure and formation energy of the possible metastable phases of different structures is examined through MD simulations for the Ni−Nb system over the entire composition range.

II. Construction of an *n*-Body Ni−Nb Potential

The formalism developed by Finnis and Sinclair,[25] that is, the FS formalism, is adopted in the present study as a computational framework to construct the *n*-body potential of the Ni−Nb system, since it has been proven to be capable of describing the interatomic interaction involved in the body-centered cubic (bcc) and face-centered cubic (fcc) metals and alloys in a relatively satisfactory way.[26−28] In the FS formalism, the total energy of a system is given by

$$U_{\text{tot}} = \frac{1}{2}\sum_{ij} V(r_{ij}) - \sum_i \left[\sum_{i\neq j} A^2 \phi(r_{ij})\right]^{1/2} \tag{1}$$

The first term in eq 1 is a conventional central pair-potential summation, which is expressed by a hexad polynomial in the present study

$$V(r) = \begin{cases} (r-c)^2(c_0 + c_1 r + c_2 r^2 + c_3 r^3 + c_4 r^4), & r \leq c \\ 0, & r > c \end{cases} \tag{2}$$

where *c* is a disposable parameter assumed to lie between the second and third neighbor atoms. c_0, c_1, c_2, c_3, and c_4 are the

TABLE 1: Fitted Parameters of the *n*-Body Potentials for the Ni−Nb System

	Ni−Ni	Nb−Nb	Ni−Nb
A (eV·Å^{-1})	0.982 476 7	2.999 182	1.825 783
d (Å)	4.12	3.9	3.75
c (Å)	4.22	4.07	4.25
c_0 (eV·Å^{-2})	13.282 760	25.575 480	22.470 780
c_1 (eV·Å^{-3})	−17.085060	−26.842 730	−24.198 810
c_2 (eV·Å^{-4})	8.262 515	9.903 115	8.854 626
c_3 (eV·Å^{-5})	−1.770 480	−1.297 269	−1.098 587
c_4 (eV·Å^{-6})	0.141 390 2	0.014 288 83	0.0

TABLE 2: Comparison between Some Calculated Physical Properties Reproduced by the *n*-Body Potentials and the Experimental Values Used in Fitting the Potentials for Pure Ni and Nb (E_v^f Is the Unrelaxed Vacancy Formation Energy)

	Ni		Nb	
	experimental	calculated	experimental	calculated
E_c (eV)	4.44[a]	4.437	7.57[a]	7.572
a (Å)	3.52[a]	3.520	3.30[a]	3.300
C_{11} (Mbar)	2.45[b]	2.450	2.47[b]	2.470
C_{12} (Mbar)	1.40[b]	1.485	1.35[b]	1.347
C_{44} (Mbar)	1.25[b]	1.182	0.287[b]	0.2871
E_v^f (eV)	1.60[c]	1.624	2.75[d]	2.746

[a] Reference 29. [b] Reference 30. [c] Reference 31. [d] Reference 32.

potential parameters to be fitted. The second term in eq 1 is the *n*-body term and takes a sum form over all atoms for a cohesive function as follows:

$$\phi(r) = \begin{cases} (r-d)^2, & r \leq d \\ 0, & r > d \end{cases} \tag{3}$$

where *d* is also assumed to lie between the second and third neighbor atoms. Obviously, there is a total of eight potential parameters, that is, A, c, d, c_0, c_1, c_2, c_3, and c_4, to be fitted. For a perfect crystal, in which all the atoms are equivalent, the cohesive energy (E_c) is equal to the negative value of the energy per atom and can therefore be expressed as

$$E_c = A\sum_{i\neq 0}\sqrt{\phi(r_i)} - \frac{1}{2}\sum_{i\neq 0} V(r_i) \tag{4}$$

For a binary alloy, $A_x B_{(1-x)}$, one can obtain the cohesive energy (E_{AB}) by the following equation:

$$E_{AB} = -[xE_A + (1-x)E_B] \tag{5}$$

where E_A and E_B are the energies per atom A and B, respectively, in the $A_x B_{(1-x)}$ alloy.

The potential parameters for pure Ni and Nb are determined by fitting the experimental data of cohesive energy (E_c), lattice constant (a), elastic constants (C_{11}, C_{12}, and C_{44}), and the fitted potential parameters are listed in Table 1. The procedure of parametrization is similar to that described by Finnis and Sinclair.[25] The physical properties reproduced from the derived Ni and Nb potentials and the corresponding experimental data used in fitting are listed in Table 2. From Table 2, one can see that the derived Ni and Nb potentials work fairly well in reproducing some physical properties of the pure Ni and Nb, respectively.

As there are very few available experimental data related to the Ni−Nb compounds, it is a challenging task to fit the Ni−Nb cross-potential. In this respect, the first-principles calculation based on quantum mechanics is known to be a reliable way to acquire some physical properties of the alloy phases of

TABLE 3: Comparison of the Cohesive Energy (E_c, eV) and Lattice Constant (a, Å) Derived from the Constructed Ni−Nb Potential versus Those from Experiments/ab Initio Calculation[a]

system	structure[b]	ab initio calculation		present study		experimental
Ni₃Nb	L1₂	E_c = 5.361	a = 3.690	E_c = 5.230	a = 3.651	
	D0₁₉	E_c = 5.478	a = 2.625	E_c = 5.227	a = 2.603	a = 2.60[c]
					c/a = 1.62	c/a = 1.62[c]
NiNb	B2	E_c = 6.026*	a = 3.090*	E_c = 6.026	a = 3.090	
NiNb₃	L1₂	E_c = 6.692*	a = 4.050*	E_c = 6.698	a = 4.115	a = 4.11[d]
	D0₁₉	E_c = 6.648	a = 2.875	E_c = 6.698	a = 2.911	

[a] Note that, for the D0₁₉ structures, the values of c/a are optimized. For D0₁₉ Ni₃Nb, c/a = 1.62, and for D0₁₉ NiNb₃, c/a = 1.63. The data used in fitting are denoted by asterisks. [b] Reference 41. [c] Reference 42. [d] Reference 43.

TABLE 4: Calculated Lattice Constants (a) and Cohesive Energies (E_c) of Ni and Nb in Three Simple Structures (fcc, hcp, and bcc)

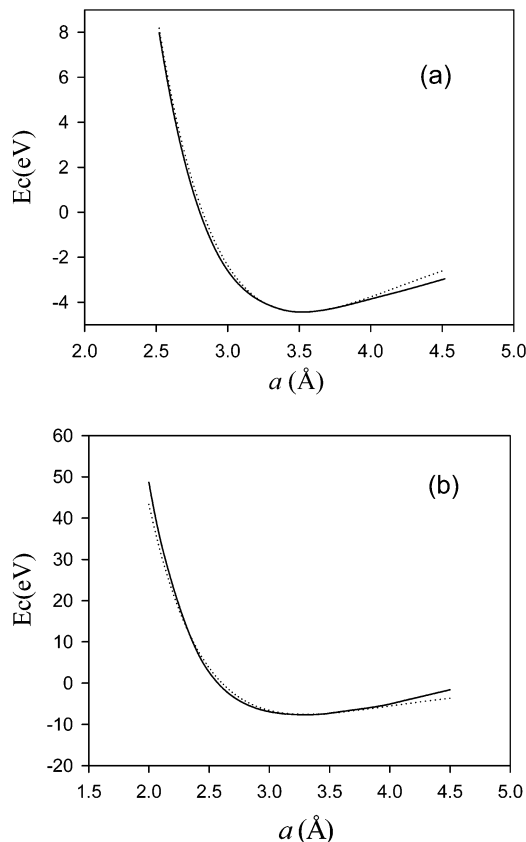|	Ni		Nb	
structure	a (Å)	E_c (eV)	a (Å)	E_c (eV)
fcc	3.520	4.437	4.218	7.247
hcp	2.488	4.436	2.983	7.247
bcc	2.788	4.357	3.300	7.572

interest.[33−35] In the present study, the first-principles calculations are carried out using the well-established Vienna ab initio simulation package (VASP).[36,37] In the calculation, plane-wave basis and fully nonlocal Vanderbilt-type ultrasoft pseudopotentials are employed.[38] The exchange and correlation items are described by the generalized-gradient approximation (GGA) proposed by Perdew and Wang.[39] The integration in the Brillouin zone is done in a mesh of $11 \times 11 \times 11$ special k points determined according to the so-called Monkhorst−Pack scheme, as such an integration has proved to be sufficient for the computation of the simple structures.[40] The calculated results are listed in Table 3. With the calculated cohesive energies and lattice constants of the B2 NiNb and L1₂ NiNb₃ compounds, the cross-potential of Ni−Nb can be fitted, and the fitted parameters are also listed in Table 1.

To prove the relevance of the Ni and Nb potentials, we first reproduced the cohesive energies and lattice constants of the equilibrium structures and their metastable structures for pure Ni and Nb, respectively. The calculated results are listed in Table 4. From Table 4, one can clearly see that the cohesive energy of fcc Ni is greater than that of bcc Ni and that the cohesive energy of bcc Nb is greater than that of fcc Nb, reflecting well the fact that the equilibrium states of the pure Ni and Nb are fcc and bcc structures, respectively. In addition, we also compare the equation of state reproduced by the constructed potentials with Rose's equation, which is considered as a universal equation of state for metals,[44] and it turned out that they are in good agreement, as shown in Figure 1.

To test the Ni−Nb cross-potential, we employ the potential to reproduce the cohesive energies and the lattice constants of the Ni₃Nb, NiNb, and NiNb₃ metastable compounds, and the results are also listed in Table 3. In the table, the asterisks denote the values used in fitting the potential. One sees that the calculated properties from the constructed potential are in good agreement with those obtained from ab initio calculations. It is thus concluded that the newly constructed n-body Ni−Nb potential is of relevance in describing the atomic interactions in the Ni−Nb system.

III. Simulation and Characterization Methods

A. Simulation Model (1): Solid Solution Models. On the basis of the constructed Ni−Nb potential, MD simulations are carried out at a constant temperature and at 0 Pa for the fcc Ni-based and bcc Nb-based solid solution models[15] with various

Figure 1. Equation of state reproduced from the constructed Ni−Nb potential (solid line) compared with Rose's equation (dotted line): (a) Ni; (b) Nb.

solute concentrations, respectively. As the present study is mainly interested in the structural phase transition in the Ni−Nb system at room temperature, the constant temperature is set to be 300 K. The simulation models consist of $7 \times 7 \times 7 = 343$ unit cells (1372 atoms) for the fcc Ni-based solid solution and $8 \times 8 \times 8 = 512$ unit cells (1024 atoms) for the bcc Nb-based solid solution. For both solid solution models, the [100], [010], and [001] crystalline directions are parallel to the x, y, and z axes, respectively. Periodic boundary conditions are adopted in three axes. In setting the solid solution models, the solute atoms are added into the model by the random substitution of a desired number of solvent atoms to obtain the initial state of the solid solution models. In the present study, MD simulations are then carried out with the Parrinello−Rahman constant pressure scheme and the equations of motion are solved using the second-order four-value predictor−corrector algorithm of Gear with a time step of $t = 5 \times 10^{-15}$ s.[45−47] In the present study, MD simulations are conducted for 50 000−150 000 MD time steps to reach a relatively stable (i.e., metastable) state, at which all the related dynamic variables show no secular variation.

B. Simulation Model (2): Sandwich Models. To represent the multilayered samples frequently employed in IBM and solid-state reaction (SSR) experiments, we adopt a sandwich model with periodic boundary conditions in MD simulations. The sandwich model is constructed by stacking Ni(001) atomic planes and Nb(001) atomic planes along the z axis and parallel to the $x-y$ plane, and the orientations of the atomic planes were indexed by their Miller indices, for example, [6(111)Ni] refers to an Ni lattice of fcc structure stacked by six (111) atomic planes. The crystalline directions ⟨100⟩ of fcc Ni and ⟨100⟩ of bcc Nb are arranged to be parallel to the x and y axes with unit distances of 3.52 and 3.30 Å, respectively, leading to a size difference ratio of 1.067. Considering the number of the atoms in the simulation model to be within a manageable scale, the numbers of Ni and Nb unit cells in the $x-y$ plane are selected to be $11 \times 11 = 121$ and $12 \times 12 = 144$, respectively, resulting in a lattice difference ratio of $12/11 = 1.091$, which is reasonably close to the above-mentioned real situation. Periodic boundary conditions are also adopted in three axes. Obviously, such a setting would cause a misfit for the lattice dimension of Ni and result in a 2.2% density decrease of Ni in the simulation model. In this regard, Mura et al. have shown that such a small density decrease would only have a minor influence on the simulation results.[48]

In the present study, two sandwich models are constructed to simulate the solid-state interfacial reaction in the Ni−Nb system, that is, the [6(001)Nb/8(001)Ni/6(001)Nb] and [4(001)-Ni/8(001)Nb/4(001)Ni] models, which correspond to alloy concentrations of 52.84 and 62.69 atom % Ni, respectively. It will be shown later that the interfacial reactions taking place in the two sandwich models are essentially the same, regardless of whether the Ni or Nb layer is set as the interlayer.

C. Characterization Methods. The structural phase transition in the Ni−Nb solid solution and sandwich models is monitored by the pair-correlation function ($g(r)$), planar structure factor ($S(\mathbf{k},\mathbf{z})$), and density profiles of each species along the z direction ($\rho_\alpha(z)$). As one of the main criteria to determine an amorphous structure, $g(r)$ is commonly used to characterize the structure to be either crystalline or amorphous, or disordered. To calculate the pair-correlation function ($g(r)$), each atom was imagined to be at the center of a series of concentric spheres. The atomic density ($\rho(r)$) was defined to be the number of atoms in each spherical shell divided by the volume of that shell, with the consideration of those periodic images located outside the block. By averaging over all the atoms within 200 time steps, $g(r)$ can then be obtained by the following formula:

$$g(r) = \frac{\rho(r)}{\rho_0} \tag{6}$$

where $\rho(r)$ denotes the atomic density at $r = |r|$ and $r = 0$ defines the position of a reference. ρ_0 is the average atomic density in the whole model. The planer structure factor ($S(\mathbf{k},\mathbf{z})$) is a Fourier transformation of the density in each crystallographic plane parallel to the $x-y$ plane and is defined by Phillpot et al. Accordingly, it can be expressed as[49]

$$S(\mathbf{k},\mathbf{z}) = \left\langle \frac{1}{N_z^2} \left| \sum_{j=1}^{N_z} \exp(i\mathbf{k}\cdot r_j) \right|^2 \right\rangle \tag{7}$$

where $\mathbf{z}$ labels the crystal plane to which the point r_j belongs in the initial configuration and $\mathbf{k}$ is an arbitrary vector of the planar reciprocal lattice. In the present study, $\mathbf{k} = (1,1)$ is used. N_z is the number of layers perpendicular to the z axis, and the broken
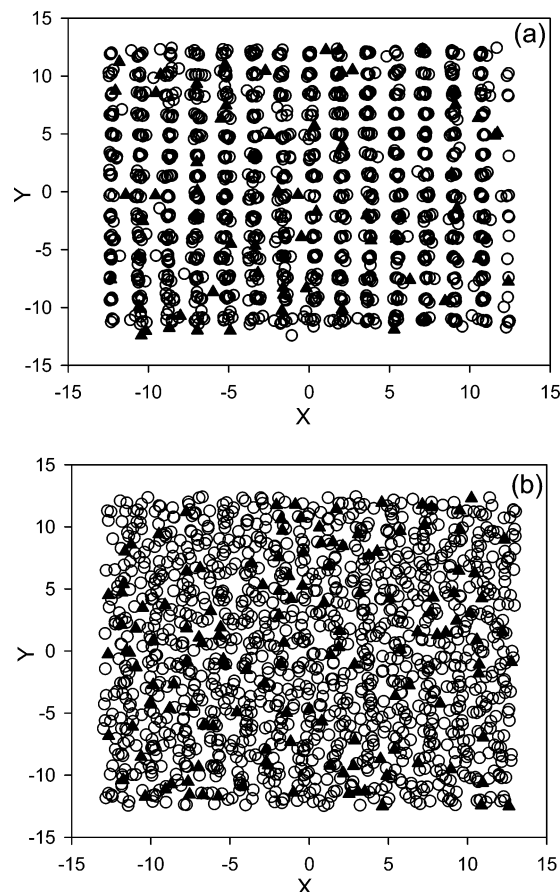

Figure 2. Projections of atomic positions for the (a) Ni$_{91}$Nb$_9$ and (b) Ni$_{87}$Nb$_{13}$ solid solutions after annealing at 300 K for 100 000 MD time steps. Open circles, Ni; filled triangles, Nb.

brackets mean that $S(\mathbf{k},\mathbf{z})$ is an average value obtained within some time steps in the MD simulation. Accordingly, the planar structure factor $S = 1$ refers to an entirely ordered crystal, while $S = 0$ is for a completely disordered state. The density profiles ($\rho_\alpha(z)$) of each species along the z direction are also calculated to define the position of a single atomic layer, indicating the local (i.e., restricted to the single layer) structural and compositional properties of the models.[50]

IV. Results and Discussion

A. Crystal-to-Amorphous Transition and the Intrinsic Glass-Forming Ability. We now present the simulation results for the fcc Ni-based solid solution models first. It has been estimated that the error of solid solubility determined by MD simulation is ∼3−5 atom %;[10] therefore, we vary the solute concentration with an interval of 4 atom % to determine the critical solid solubility. Figure 2 displays the projections of atomic positions for the Ni$_{91}$Nb$_9$ and Ni$_{87}$Nb$_{13}$ fcc solid solutions after annealing at 300 K for 100 000 MD time steps, respectively. From Figure 2, one sees vividly that, for the solid solution with 9 atom % Nb, the fcc structure can be clearly visualized; that is, it still remains in its original fcc crystalline structure, while, for the solid solution with 13 atom % Nb, the lattice has apparently collapsed and turned into a disordered state; that is, a crystal-to-amorphous transition has obviously taken place. Figure 3 shows the corresponding density profiles ($\rho_\alpha(z)$) for the solid solutions with the alloy compositions Ni$_{91}$Nb$_9$, Ni$_{87}$-Nb$_{13}$, and Ni$_{80}$Nb$_{20}$, respectively. It can be seen that, when the solute concentration is <13 atom % Nb, the atomic planes can clearly be distinguished from the density profiles; however, once
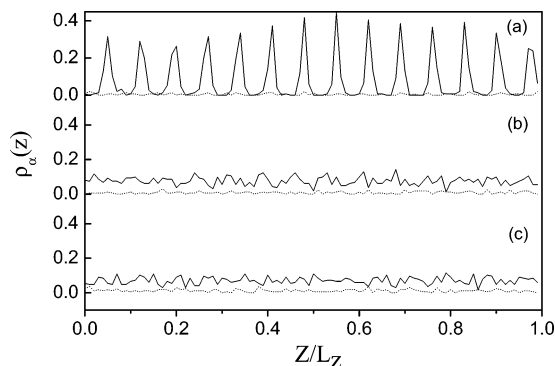
Atomistic Modeling of Crystal-to-Amorphous Transition

J. Phys. Chem. B, Vol. 109, No. 10, 2005 **4721**

Figure 3. Calculated density profiles ($\rho_\alpha(z)$) of Ni and Nb atoms along the z direction in (a) $Ni_{91}Nb_9$, (b) $Ni_{87}Nb_{13}$, and (c) $Ni_{80}Nb_{20}$ solid solutions after annealing at 300 K for 100 000 MD time steps. $\rho_{Ni}(z)$ is represented by the solid line and $\rho_{Nb}(z)$ by the dotted line. The ordinate is in arbitrary units.
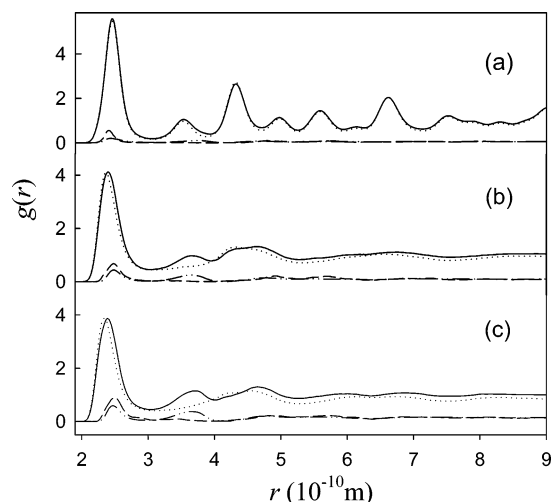

Figure 4. Total and partial pair-correlation functions for the fcc Ni-rich solid solutions after annealing at 300 K for 100 000 MD time steps. The compositions of the solid solutions are (a) 9 atom %, (b) 13 atom %, and (c) 20 atom % Nb. The solid line is for the total $g(r)$, the short-dashed line is for the Nb–Nb partial $g(r)$, the dotted line is for the Ni–Ni partial $g(r)$, and the dash–dot–dotted line is for the Ni–Nb partial $g(r)$.

the Nb concentration equals or exceeds 13 atom %, a relatively uniform distributed density profile appears. To have firm evidence, the total and partial pair-correlation functions ($g(r)$) for fcc Ni-based solid solutions are calculated and shown in Figure 4. In the figure, as the $g(r)$ curve of $Ni_{91}Nb_9$ remains apparent sharp peaks even at a large distance r, the $Ni_{91}Nb_9$ simulation model is still in a crystalline structure. Whereas for the $Ni_{87}Nb_{13}$ and $Ni_{80}Nb_{20}$ simulation models, the $g(r)$ curves become more or less smooth and the peaks, except for the first one, even disappear, indicating that a crystal-to-amorphous transition takes place when the Nb concentration equals or exceeds 13 atom % in the Ni-rich solid solutions. In fact, all the simulation models with Nb solute concentrations exceeding 13 atom % show obvious amorphous characteristics in their $\rho_\alpha(z)$ and $g(r)$ figures; therefore, only a typical model, $Ni_{80}Nb_{20}$, is given in the figures. It is noted that the calculated curves of the $Ni_{87}Nb_{13}$ and $Ni_{80}Nb_{20}$ simulation models are similar, as shown in Figures 3 and 4, respectively, implying that they have similar amorphous structures.

From the above results, it can be concluded that the critical solid solubility is 13 atom % Nb for the fcc Ni-based solid solutions. Note that the equilibrium solid solubility of Nb in Ni at low temperatures, for example, at 400 K, is ~2–3 atom %,[51]
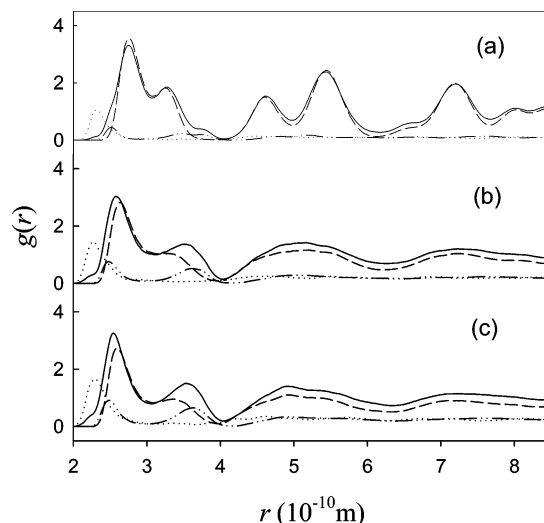

Figure 5. Total and partial pair-correlation functions for the fcc Nb-rich solid solutions after annealing at 300 K for 100 000 MD time steps. The compositions of the solid solutions are (a) 15 atom %, (b) 19 atom %, and (c) 25 atom % Ni. The solid line is for the total $g(r)$, the short-dashed line is for the Nb–Nb partial $g(r)$, the dotted line is for the Ni–Ni partial $g(r)$, and the dash–dot–dotted line is for the Nb–Ni partial $g(r)$.

indicating that, under nonequilibrium conditions, the solid solubility could be significantly extended. Apparently, the Ni-based solid solution containing 13 atom % Nb is therefore a supersaturated one. According to the thermodynamics of solids, the supersaturated Ni-based solid solution is in a metastable state and the higher the concentration of Nb is, the less stable the supersaturated solid solution is. Once the concentration of Nb exceeds the critical solid solubility, the solid solution would become unstable and turn into a disordered state, resulting in a crystal-to-amorphous transition. In other words, the physical origin of crystal-to-amorphous transition is the crystalline lattice collapsing while the solute atoms are exceeding the critical value. From an energetic point of view, when the concentration reaches or exceeds the critical solid solubility, the formation of an amorphous alloy is favored compared with the corresponding supersaturated solid solution of fcc structure.

Similarly, for the bcc Nb-based solid solution, the critical solid solubility is determined to be 19 atom % Ni, which is also considerably greater than the equilibrium value of around 5 atom % Ni in Nb.[51] Figure 5 displays the $g(r)$ curves for the Nb-rich bcc solid solutions with three different alloy compositions. Apparently, the $g(r)$ curves feature a bcc crystalline structure when the Ni concentration is <19 atom % Ni, whereas when the Ni concentration exceeds the critical solid solubility, the $g(r)$ curves are typical of an amorphous structure. We also calculated the atomic projections of the x–z plane and the density profiles ($\rho_\alpha(z)$) of the Ni and Nb atoms along the z direction, and the calculated results all confirm that the supersaturated solid solution would collapse and turn into a disordered state when the concentration of Ni reaches or exceeds ~19 atom % Ni. It should be noted that, either in Figure 4 or in Figure 5, the height of the first peak changes slightly with increasing solute concentration, implying that the number of the first neighbor atoms in either the crystalline or amorphous state almost stays unchanged and that, in a short-range region, the amorphous state also features some ordering behavior.

From the above results, one can see that there are two critical solid solubilities: one is 13 atom % Nb for the fcc Ni-based solid solution, and the other is 19 atom % Ni for the bcc Nb-based solid solution. For the Ni–Nb system, an amorphous alloy
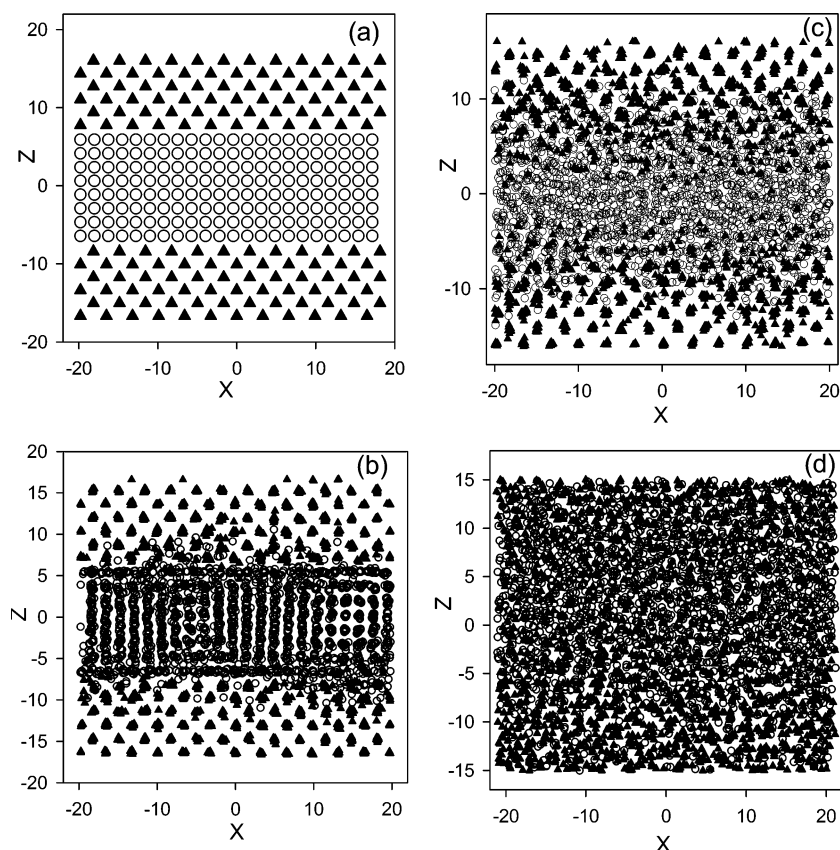
Figure 6. Projections of atomic positions on the x–z plane of the [6(001)Nb/8(001)Ni/6(001)Nb] sandwich model upon isothermal annealing at 573 K for (a) 0 time steps, (b) 15 000 time steps, (c) 70 000 time steps, and (d) 300 000 time steps. Open circles, Ni; filled triangles, Nb.

would form when its composition falls into the composition range bounded by the two determined critical solid solubilities. It is therefore concluded that the glass-forming ability/range (GFA/GFR) of tthe Ni–Nb system is ∼19–87 atom % Ni according to the present study. It is important to compare the above simulation results with other theoretical results as well as the experimental observations. For instance, by comparing the Gibbs free energies of the crystalline and amorphous phases of the Ni–Nb alloys, Gallego et al. have determined the GFR of the Ni–Nb system to be within 20–80 atom % Ni,[52] which falls in the GFR, that is, 19–87 atom % Ni, determined directly from the newly derived Ni–Nb potential through MD simulation. In IBM experiments conducted by Zhang et al.,[4] amorphous alloys were readily formed within a composition range of 20–85 atom % Ni, which also falls in the GFR determined by the present simulation. In short, the GFR determined from the interatomic potential through MD simulation matches well with other theoretical results as well as the experimental observations.

From a physical point of view, the GFR determined in the present study is directly calculated from the interatomic potential, which governs the atomic configurations, thus also governing the energetic states, of both solid solutions and the competing disordered states. The GFR thus determined can therefore be considered as an intrinsic property of a system and has nothing to do with any practically applied glass-producing technique. Comparatively, the experimentally measured GFR should then be considered as a nominal one, which depends on the specific glass-producing technique applied in practice. It is therefore deduced that the GFR measured in IBM experiments could be a little narrower than that determined by the potential. Clearly, one can see that the GFR determined in the present study is consistent with that obtained from IBM experiments,

which, in turn, provides additional evidence for the relevance of the n-body potential constructed in the present study.

B. Asymmetric Growth Kinetics in Solid-State Interfacial Reaction. We now present the simulation results using the sandwich models for studying the growth kinetics of SSA in the Ni–Nb multilayers. Figure 6a shows the initial state of the sandwich model, in which the Ni and Nb crystalline lattices are sharply separated by two interfaces. The model is then isothermally annealed at 573 K. Parts b, c, and d of Figure 6 display three snapshots of the projections of the atomic positions on the x–z plane after isothermal annealing for 15 000, 70 000, and 300 000 time steps, respectively. From Figure 6, one can find that the layers near the interface are disordered at 15 000 MD time steps and gradually extend outward with increasing time and that after 300 000 time steps, the disordered interlayers extend throughout the model, resulting in a uniform amorphous structure. By a close inspection of Figure 6, one can see that the Ni–Nb disordered region at the interfaces extends in a layer-by-layer mode. Figure 6c shows that all the Ni atomic planes have become disordered, while most of the Nb atomic planes still remain in crystalline structures. Figure 6b and c also indicates that the Ni lattice near the interlayer became disordered earlier than that of the Nb lattice next to the interlayer and that the extension/growth of the disordered region is faster toward the Ni lattice than that toward to the Nb side, exhibiting an asymmetric growth behavior of the amorphous interlayer during SSA taking place in the Ni–Nb system.

Figure 7 shows the changes of the density profiles ($\rho_\alpha(z)$) of each species along the z direction, perpendicular to the interface, upon isothermal annealing at 573 K with increasing time steps. One sees that mutual diffusion, which is defined as the migration of Ni and Nb atoms crossing the interface, does take place at
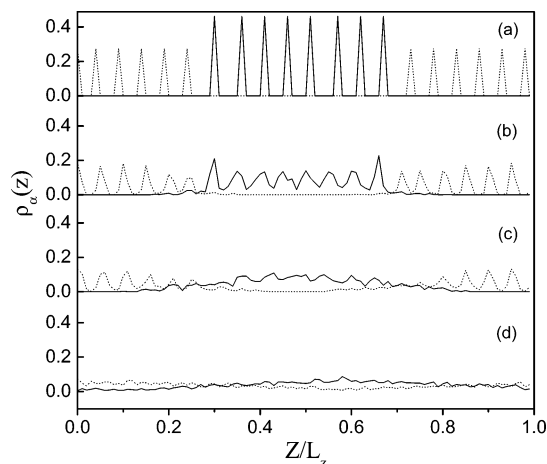
Atomistic Modeling of Crystal-to-Amorphous Transition

J. Phys. Chem. B, Vol. 109, No. 10, 2005 **4723**

Figure 7. Calculated density profiles ($\rho_\alpha(z)$) of each species along the z direction, perpendicular to the interface, for (a) the initial state and the states obtained after annealing at 573 K for (b) 15 000, (c) 70 000, and (d) 300 000 time steps in the [6(001)Nb/8(001)Ni/6(001)-Nb] sandwich model. $\rho_{Ni}(z)$ is represented by the solid line and $\rho_{Nb}(z)$ by the dotted line. The ordinate is in arbitrary units.

573 K and that the amount of atomic diffusion increases with increasing simulation time, resulting eventually in the uniformly distributed density profiles ($\rho_\alpha(z)$) of both Ni and Nb along the z direction at 300 000 time steps. In Figure 7a and b, one can see that the $\rho_\alpha(z)$ of either Ni or Nb has obvious peaks, indicating that Ni and Nb are both in crystalline structures. However, in Figure 7c, one can see that the $\rho_\alpha(z)$ of Ni has become uniformly distributed, while that of Nb still retains obvious crystalline peaks after annealing at 573 K for 70 000 time steps, confirming the appearance of asymmetric growth during interfacial reaction in the Ni−Nb multilayers. Furthermore, the planar structure factors ($S(\mathbf{k},\mathbf{z})$) are calculated for the 20 atomic planes and they decrease from ∼0.99 in the initial state to <0.1 after 300 000 time steps, confirming that the whole sandwich model has become completely disordered.

To further characterize the asymmetric growth during isothermal annealing, the partial and total pair-correlation functions for the Ni region (nos. 7−14 atomic planes) and the Nb region (nos. 1−6 atomic places) are calculated, respectively, after annealing at 573 K for 70 000 time steps, and they are shown in Figure 8. From the figure, one observes that, in the Ni region, the Ni−Ni $g(r)$ shows the shape commonly known for a typical amorphous phase, while, in the Nb region, the crystalline peaks of Nb−Nb $g(r)$ still remain, suggesting that the structure of Nb is more stable than that of Ni and the disordering speed of the Ni lattice is faster than that of the Nb lattice; that is, an asymmetric growth does take place during the process of SSA in the Ni−Nb multilayers. In addition, on the basis of the $S(\mathbf{k},\mathbf{z})$, $\rho_\alpha(z)$, and $g(r)$ calculated at various annealing times, the thicknesses (X) of the growing amorphous interlayer toward the Ni and Nb lattices, respectively, are monitored as a function of the annealing time (t), and the results are shown in Figure 9. From the figure, one sees that the disordering process toward Ni is obviously faster than that directed toward Nb, as the Ni fcc structure has become an amorphous state completely, while only two atomic planes of the Nb bcc structure have become disordered. To further examine the conclusion, we also perform MD simulations for another sandwich model of [4(001)Ni/8(001)Nb/4(001)Ni] upon isothermal annealing at 573 K, and similar results are obtained. As an example, Figure 9 also shows the correlations between the growth thicknesses (X) of the amorphous interlayer toward the Ni and Nb lattices, respectively, and annealing time (t) in the sandwich model. Apparently, the
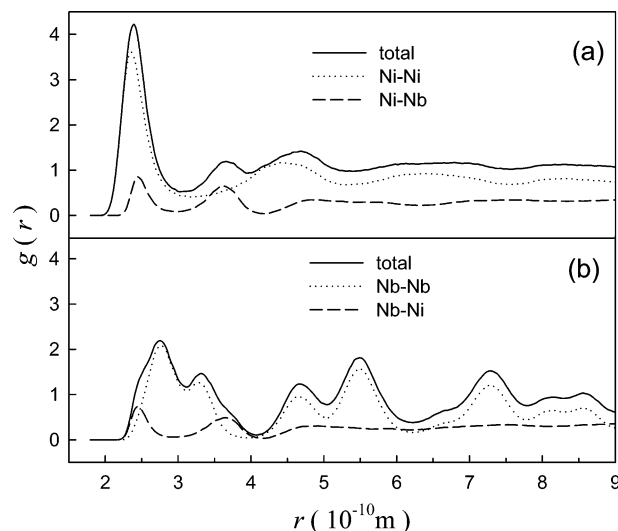

Figure 8. Total and partial pair-correlation functions for the (a) nos. 7−14 atomic planes and (b) nos. 1−6 atomic planes in the [6(001)-Nb/8(001)Ni/6(001)Nb] sandwich model upon isothermal annealing at 573 K for 70 000 MD time steps.
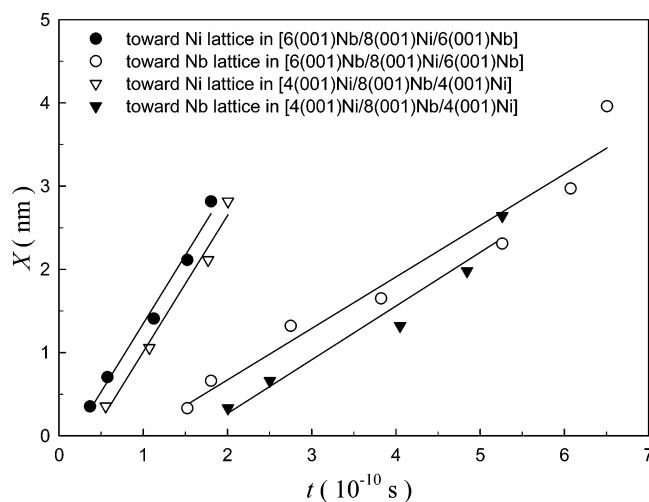

Figure 9. Growing thicknesses (X) of the amorphous interlayer as a function of annealing time (t) toward the Ni and Nb lattices, respectively, in the [6(001)Nb/8(001)Ni/6(001)Nb] and [4(001)Ni/8(001)Nb/4(001)Ni] sandwich models upon isothermal annealing at 573 K.

disordering process toward Ni is faster than that directed to Nb, indicating that asymmetric growth also took place in the model. Note that, in the first sandwich model, there are 12 Nb atomic layers, whereas, in the second sandwich model, there are 8 Nb atomic layers. Such a difference makes the second sandwich model become completely disordered in a shorter time than the first model does (see Figure 9). Nonetheless, similar asymmetric growth behaviors are revealed in both sandwich models, meaning that the simulation results are not affected by the stacking sequence of Ni and Nb in the sandwich models, that is, either by Ni/Nb/Ni or by Nb/Ni/Nb.

Experimentally, the asymmetric growth behavior of the amorphous interlayer has been observed in the Ni−Nb multilayers upon solid-state interfacial reaction.[23] Actually, the asymmetric growth kinetics can be well understood in terms of the physical origin of the crystal-to-amorphous transition revealed by the above MD simulations. We have determined that 19 atom % Ni solute atoms are necessary to destabilize and transform the Nb bcc solid solution into an amorphous state, whereas the critical concentration for the Ni solid solution is
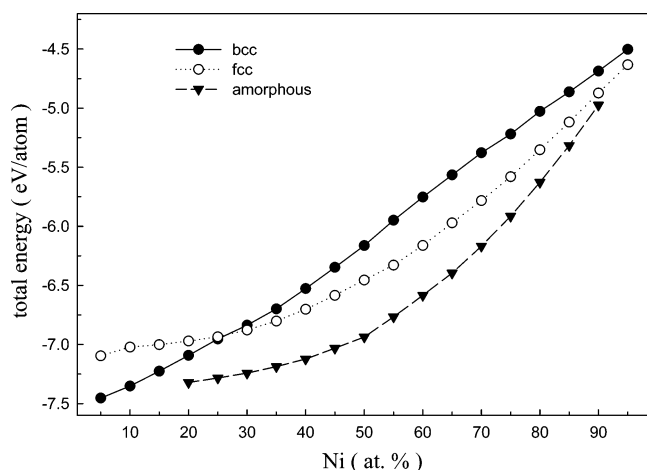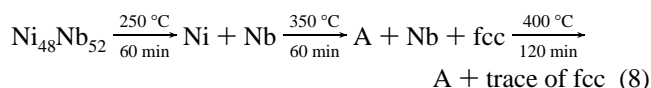
Figure 10. Calculated total energies of the Ni−Nb phases in different structures versus the Ni composition over the entire composition range. The values of the fcc and bcc Ni−Nb phases are obtained at 300 K from the fcc and bcc solid solution models, respectively. The values of the amorphous Ni−Nb phases in the ranges 19−50 and 50−87 Ni atom % are obtained from the bcc and fcc solid solution models, respectively, upon isothermal annealing at 300 K for 100 000 MD time steps.

~13 atom % Nb. Apparently, the critical composition of the fcc Ni is lower that that of the bcc Nb, which implies that the fcc Ni layers in the bilayer or the multilayer will approach and exceed the critical value faster than the Nb layer. Therefore, the Ni lattice is much easier to amorphize than the Nb lattice.

C. Structural Stability of the Metastable Ni−Nb Phases. On the basis of the constructed potential, the structural stability of the metastable Ni−Nb phases over the entire composition range can also be studied. Accordingly, we perform MD simulations to determine the energies of the fcc and bcc solid solutions, respectively, over the entire composition range as well as the energies of the amorphous phase in the above determined GFR of 19−87 atom % Ni. Consequently, an energy diagram for the metastable Ni_xNb_{100-x} phases is obtained and shown in Figure 10. In the figure, all the fcc and bcc solid solutions apparently have higher energies than their amorphous counterparts when $19 \leq x \leq 87$ and there appears to be a thermodynamic driving force for the formation of the amorphous alloys within this composition range. Obviously, the calculated energetic sequence comparing solid solutions and the amorphous phases is quite compatible with what was shown in determining the GFR by MD simulations using both fcc and bcc solid solution models. Besides, the fcc Ni_xNb_{100-x} phase has a lower energy than the bcc phase when $30 \leq x \leq 100$, while the bcc phase is more stable than the fcc phase when $0 \leq x \leq 25$. Interestingly, regarding the energetic sequence of the metastable Ni−Nb phases, there have been some experimental observations which are in good agreement with the above simulation results. For instance, the following structural evolution process has been observed in the $Ni_{48}Nb_{52}$ multilayered films upon thermal annealing:[23]

$$Ni_{48}Nb_{52} \xrightarrow[60\ min]{250\ °C} Ni + Nb \xrightarrow[60\ min]{350\ °C} A + Nb + fcc \xrightarrow[120\ min]{400\ °C}$$
$$A + trace\ of\ fcc \quad (8)$$

where A is the amorphous state and fcc refers to a metastable phase with fcc structure. Apparently, the observed structural evolution process is quite compatible with the simulation results. Besides, in IBM experiments, the following structural evolution process has been observed in the $Ni_{70}Nb_{30}$ multilayered films:[4]

$$Ni_{70}Nb_{30} \xrightarrow{3 \times 10^{14}} hcp \xrightarrow{3 \times 10^{15}} A \quad (9)$$
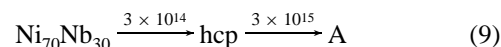
It should be pointed out that fcc and hcp structures are similar close-packed structures and their energy difference is very little, which has been proved by thermodynamics calculation.[53] Consequently, the above structural evolution process is also compatible with the present simulation results. The good compatibility of these experimental observations with the present simulation results suggests that the calculated energy diagram from the Ni−Nb potential through MD simulations is of relevance, which in turn confirms the validation of the newly constructed Ni−Nb potential.

To compare the simulated results with those deduced from the calculations based on the thermodynamics of solids, we also calculate the heats of formation (ΔH_f) of the metastable Ni_xNb_{100-x} phases over the entire composition range. Figure 11 shows the calculated ΔH_f values versus the Ni concentration for the metastable fcc and bcc and amorphous Ni_xNb_{100-x} phases. From the figure, one sees clearly that the fcc structure is more likely to be formed than the bcc structure in a Ni concentration of $30 \leq x \leq 100$, while the bcc structure is energetically preferred within a composition range of $0 \leq x \leq 25$. Moreover, within the composition range $19 \leq x \leq 87$, an amorphous state has a lower ΔH_f value than its fcc or bcc counterpart. It is noted that the calculated heats of formation are also compatible with those derived from Miedema's theory;[54] that is, the minimum ΔH_f value appears somewhere near the equatomic stoichiometry and the ΔH_f value increases gradually while varying the alloy composition toward the two terminals. Especially, the present computational results indicate that a very negative heat of formation exists (i.e., minimum $\Delta H_f = -89.88$ kJ/mol) for the Ni−Nb amorphous state and such a large negative heat of formation is the major driving force for solid-state interfacial reaction as well as crystal-to-amorphous transition in the Ni−Nb system.

V. Conclusion

(1) With the important aid of ab initio calculations, an *n*-body potential is constructed for the Ni−Nb system based on the Finnis−Sinclair formalism. The constructed potential works fairly well in reproducing some physical properties obtained by experiments/ab initio calculations, and the equation of state derived from the potential is in good agreement with Rose's equation.

(2) On the basis of the constructed Ni−Nb potential, molecular dynamics simulations using solid solution models reveal that the physical origin of crystal-to-amorphous transition is the crystalline lattice collapsing while the solute atoms are exceeding the critical value and determine the glass-forming range of the Ni−Nb system to be within 19−87 atom % Ni, which is quite compatible with that observed by ion beam mixing experiments.

(3) On the basis of the constructed Ni−Nb potential, molecular dynamics simulations using sandwich models reveal an asymmetric growth behavior of the amorphous interlayer during solid-state amorphization; that is, the growing speed of the amorphous interlayer toward the Ni lattice is faster than that directed toward the Nb lattice, which is quite compatible with that observed in experiments.

(4) On the basis of the constructed Ni−Nb potential, molecular dynamics simulations are performed to calculate the energies of the alloy phases of interest, and the results show that, when $0 \leq x \leq 25$, the bcc Ni_xNb_{100-x} phase has a lower ΔH_f value and is more stable than the fcc phase and that, when

Atomistic Modeling of Crystal-to-Amorphous Transition

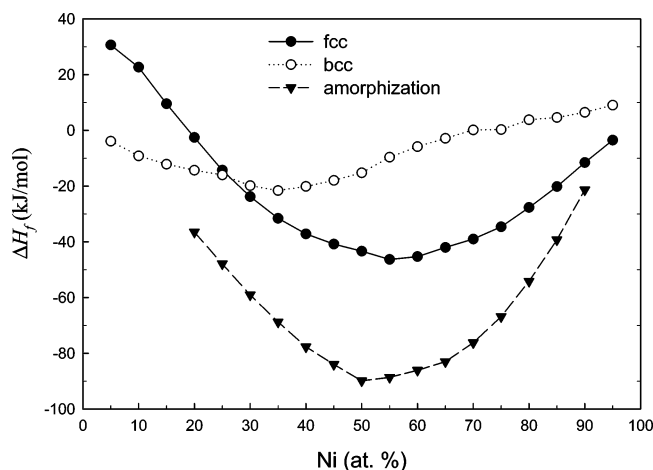*J. Phys. Chem. B, Vol. 109, No. 10, 2005* **4725**

Figure 11. Calculated heats of formation (ΔH_f) of the metastable fcc and bcc and amorphous Ni−Nb phases, respectively, versus the Ni composition over the entire composition range. The values of the fcc and bcc Ni−Nb phases are obtained at 300 K from the fcc and bcc solid solution models, respectively. The values of the amorphous Ni−Nb phases in the ranges 19−50 and 50−87 Ni atom % are obtained from the bcc and fcc solid solution models, respectively, upon isothermal annealing at 300 K for 100 000 MD time steps.

$30 \leq x \leq 100$, the fcc Ni_xNb_{100-x} phase becomes energetically favored. In addition, all the fcc and bcc phases have higher energies than their amorphous counterparts in a composition range of $19 \leq x \leq 87$, which matches well with the GFR determined by molecular dynamics simulations using solid solution models.

References and Notes

(1) Klement, W.; Willens, R. H.; Duwez, P. *Nature* **1960**, *187*, 869.
(2) Zallen, Z. *The Physics of Amorphous Solid*; Wiley-Interscience: New York, 1983.
(3) Greer, A. L. *Science* **1995**, *267*, 1947.
(4) Zhang, Z. J.; Bai, H. Y.; Qiu, Q. L.; Yang, T.; Tao, K.; Liu, B. X. *J. Appl. Phys.* **1993**, *73*, 1702.
(5) Liu, B. X.; Ou, J. *Phys. Status Solidi A* **1997**, *161*, 3.
(6) Li, J. H.; Guo, H. B.; Kong, L. T.; Liu, B. X. *Phys. Rev. B* **2005**, *71*, 014107.
(7) Alonso, J. A.; Simozar, S. *Solid State Commun.* **1983**, *48*, 765.
(8) Egami, T.; Waseda, Y. *J. Non-Cryst. Solids* **1984**, *64*, 113.
(9) Lopez, J. M.; Alonso, J. A.; Gallego, L. J. *Phys. Rev. B* **1987**, *36*, 3716.
(10) Lai, W. S.; Li, Q.; Lin, C.; Liu, B. X. *Phys. Status Solidi B* **2001**, *227*, 503.
(11) Lai, W. S.; Zhang, Q.; Liu, B. X. *Philos. Mag. Lett.* **2001**, *81*, 45.
(12) Liu, B. X. *Mater. Lett.* **1987**, *5*, 322.
(13) Gary, W. *Prog. Surf. Sci.* **1989**, *32*, 211.

(14) Ossi, P. M. *Phys. Status Solidi A* **1990**, *119*, 563.
(15) Liu, B. X.; Lai, W. S.; Zhang, Z. J. *Adv. Phys.* **2001**, *50*, 367.
(16) Schwarz, R. B.; Johnson, W. L. *Phys. Rev. Lett.* **1983**, *51*, 415.
(17) Zhang, Q.; Lai, W. S.; Liu, B. X. *Phys. Rev. B* **1998**, *58*, 14020.
(18) Kwon, K. W.; Lee, H. J.; Sinclair, R. *Appl. Phys. Lett.* **1999**, *75*, 935.
(19) Gong, H. R.; Kong, L. T.; Lai, W. S.; Liu, B. X. *Phys. Rev. B* **2002**, *66*, 104204.
(20) Meng, W. J.; Fultz, B.; Ma, E.; Johnson, W. L. *Appl. Phys. Lett.* **1987**, *51*, 661.
(21) Schröder, H.; Samwer, K.; Koster, U. *Phys. Rev. Lett.* **1985**, *54*, 197.
(22) Zhang, Q.; Lai, W. S.; Liu, B. X. *J. Non-Cryst. Solids* **2000**, *261*, 137.
(23) Yang, G. W.; Lin, C.; Liu, B. X. *Mater. Sci. Eng., B* **1999**, *65*, 139.
(24) Zhang, Q.; Lai, W. S.; Yang, G. W.; Liu, B. X. *J. Phys.: Condens. Matter* **2000**, *12*, 6991.
(25) Finnis, M. W.; Sinclair, J. E. *Philos. Mag. A* **1984**, *50*, 45.
(26) Yan, M.; Vitek, V.; Chen, S. P. *Acta Mater.* **1996**, *44*, 4351.
(27) Rebonato, R.; Welch, D. O. *Philos. Mag. A* **1989**, *60*, 649.
(28) Koleske, D. D.; Sibener, S. J. *Surf. Sci.* **1993**, *290*, 179.
(29) Kittel, C. *Introduction to Solid state Physics*, 7th ed.; John Wily & Sons: New York, 1996.
(30) Cohen, E. R.; Lide, D. R.; Trigg, G. L. *AIP Physics Desk Reference*, 3rd ed.; Springer: New York, 2003.
(31) Wycisk, W.; Feller-Knipmeier, M. *J. Nucl. Mater.* **1978**, *69−70*, 616.
(32) Maier, K.; Peo, M.; Saile, B.; Schaefer, H. E.; Seeger, A. *Philos. Mag. A* **1979**, *40*, 701.
(33) Luzzi, D. E.; Yan, M.; Šob, M.; Vitek, V. *Phys. Rev. Lett.* **1991**, *67*, 1894.
(34) Yan, M.; Šob, M.; Luzzi, D. E. Vitek, V.; Ackland, G. J.; Methfessel, M.; Rodriguez, C. O. *Phys. Rev. B* **1993**, *47*, 5571.
(35) Siegl, R.; Yan, M.; Vitek, V. *Modell. Simul. Mater. Sci. Eng.* **1997**, *5*, 105.
(36) Kresse, G.; Hafner, J. *Phys. Rev. B* **1993**, *47*, 558.
(37) Kresse, G.; Furthmuller, J. *Phys. Rev. B* **1996**, *54*, 11169.
(38) Vanderbilt, D. *Phys. Rev. B* **1990**, *41*, 7892.
(39) Perdew, J.; Wang, Y. *Phys. Rev. B* **1992**, *45*, 13244.
(40) Liu, J. B.; Liu, B. X. *Phys. Rev. B* **2001**, *63*, 132204.
(41) Brandes, E. A.; Brook, G. B. *Smithells Metals Reference Book*, 7th ed.; Butterworth-Heinemann: Oxford, U.K., 1992.
(42) Zhang, Z. J.; Huang, X. Y.; Zhang, Z. X. *Acta Mater.* **1998**, *46*, 4189.
(43) Zhang, Z. J.; Liu, B. X. *J. Appl. Phys.* **1994**, *75*, 4948.
(44) Rose, J. H.; Smith, J. R.; Guinea, F.; Ferrante, J. *Phys. Rev. B* **1984**, *29*, 2963.
(45) Parrinello, M.; Rahman, A. *J. Appl. Phys.* **1981**, *52*, 7182.
(46) Allen, M. P.; Tildesley, D. J. *Computer Simulation of Liquids*; Clarendon: Oxford, U.K., 1986.
(47) Ciccotti, G.; Hoover, W. G. *Molecular-Dynamics Simulation of Statistical-Mechanical Systems*; North-Holland: Amsterdam, The Netherlands, 1986.
(48) Mura, P.; Demontis, P.; Suffritti, G. B.; Rosato, V.; Vittori Antisari, M. *Phys. Rev. B* **1994**, *50*, 2850.
(49) Phillpot, S. R.; Yip, S.; Wolf, D. *Comput. Phys.* **1989**, *3*, 20.
(50) Rosato, V.; Ciccotti, G.; Pontikis, V. *Phys. Rev. B* **1986**, *33*, 1860.
(51) Okamoto, H.; Massalski, T. B. *J. Phase Equilib.* **1992**, *13*, 444.
(52) Gallego, L. J.; Somaza, J. A.; Alonso, J. A.; Lopez, J. M. *J. Phys. F: Met. Phys.* **1988**, *18*, 2149.
(53) Yang, G. W.; Lin, C.; Liu, J. B.; Liu, B. X. *J. Phys. D: Appl. Phys.* **1999**, *32*, 79.
(54) Boer, F. R.; Boom, R.; Mattens, W. C. M.; Miedema, A. R.; Niessen, A. K. *Cohesion in Metals-Transition Metal Alloys*; North-Holland: Amsterdam, The Netherlands, 1988.